🔓**Open Access**

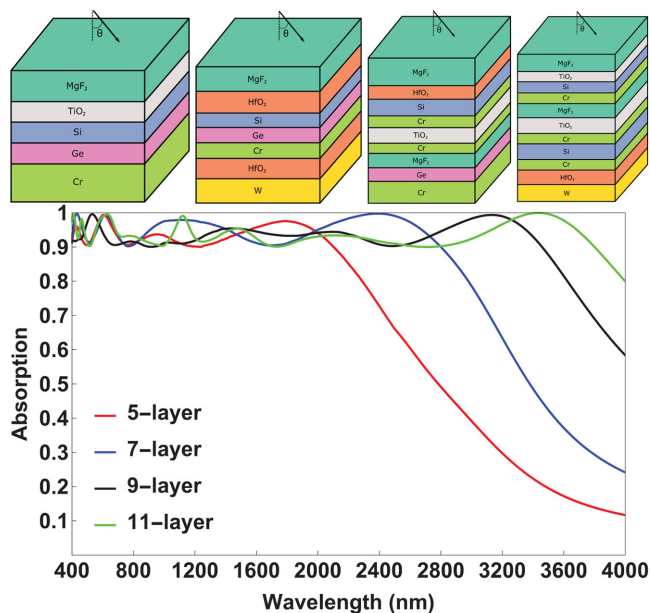# Optimized Multilayer Structures With Ultrabroadband Near-Perfect Absorption

Chenglong You
Corey T. Matyas
Yin Huang
Jonathan P. Dowling
Georgios Veronis, *Member, IEEE*

Optimized Multilayer Structures With Ultrabroadband Near-Perfect Absorption

Chenglong You [ORCID],[1] **Corey T. Matyas,**[1] **Yin Huang,**[2]
Jonathan P. Dowling,[1] **and Georgios Veronis** [ORCID],[3,4] *Member, IEEE*

[1]Hearne Institute for Theoretical Physics, Department of Physics and Astronomy,
Louisiana State University, Baton Rouge, LA 70803 USA
[2]Department of Optoelectrics Information Science and Engineering, School of Physics and
Electronics, Central South University, Changsha 410012, China
[3]School of Electrical Engineering and Computer Science, Louisiana State University,
Baton Rouge, LA 70803 USA
[4]Center for Computation and Technology, Louisiana State University, Baton Rouge,
LA 70803 USA

Abstract: We present aperiodic multilayer structures with ultrabroadband near-perfect
absorption in the visible and near-infrared wavelength range. We use a hybrid optimization
algorithm coupled with the transfer-matrix method, to optimize both the material composition
and the layer thicknesses of the aperiodic multilayer structures that are composed of infinite
slabs of material above a semi-infinite substrate. In order to achieve ultrabroadband near-
perfect absorption, we consider a broad range of materials including dielectrics, metals,
and semiconductors. The optimization algorithms previously used to design ultrabroadband
near-perfect absorbers only optimized the layer thicknesses of structures with fixed material
composition. In contrast, we find that our approach of simultaneously optimizing the material
composition as well as the layer thicknesses leads to structures with broader near-perfect
absorption. For an optimized eleven-layer structure the lower and upper absorption band
edges are 400 nm and ~3800 nm, respectively. In addition, we find that, even though
the structures are optimized for normally incident light, the absorption is high in a broad
angular range within the wavelength range of interest. We also explain the physical origin of
ultrabroadband absorption in these structures. Our results will contribute to the development
of a new generation of devices for solar photovoltaics, imaging, and photodetection.

Index Terms: Nanophotonics, physical optics, absorbers.

1. Introduction

Broadband near-perfect absorbers, operating in the visible and near-infrared wavelength ranges,
have been widely investigated—due to their many potential applications in chemical sensing [1]–
[3], thermophotovoltaic energy conversion [4], [5], imaging [6], color filters [7], [8], and thermal
emitters [9]–[13]. Broadband near-perfect absorption requires almost perfect impedance matching
between the structure and air over a broad wavelength range [14]–[16]. Many structures have
been used to achieve broadband near-perfect absorption, including metamaterial-based structures

[17]–[20], and structures supporting multiple resonances [21]–[24]. One-dimensional multilayer absorbers have the advantage of the relative ease and low cost of fabrication, based on deposition methods, compared to more complex three-dimensional structures, which require lithography and etching processes. Several approaches have been used to design and optimize multilayer structures, including genetic algorithms [25]–[27], particle-swarm optimization [28], Monte Carlo approaches [29], needle optimization [30], [31], the jump method [32], artificial neural networks, and deep learning [33], [34] in combination with physical intuition [4], [15], [35].

In this paper, we present aperiodic multilayer structures with ultrabroadband near-perfect absorption in the visible and near-infrared wavelength range. This range is important for many applications related to solar photovoltaics [36], imaging [37], and photodetection [38]. We use a hybrid optimization algorithm coupled with the transfer-matrix method, to optimize both the material composition and the layer thicknesses of the aperiodic multilayer structures that are composed of infinite slabs of material above a semi-infinite substrate. In order to achieve ultrabroadband near-perfect absorption, we consider a broad range of materials including dielectrics, metals, and semiconductors. We note that optimization algorithms previously used to design ultrabroadband near-perfect absorbers only optimized the layer thicknesses of structures with fixed material composition. In contrast, we find that our approach of simultaneously optimizing the material composition as well as the layer thicknesses leads to structures with broader near-perfect absorption. We also find that the bandwidth over which near-perfect absorption is achieved increases with the number of layers. For an optimized eleven-layer structure the lower and upper absorption band edges are 400 nm and ~3800 nm, respectively. In addition, we find that, even though the structures are optimized for normally incident light, the absorption is high in a broad angular range within the wavelength range of interest. We explain the physical origin of ultrabroadband absorption in these structures.

The remainder of this paper is organized as follows. In Section II, we describe the hybrid optimization algorithm coupled with the transfer-matrix method, which we use to optimize both the material composition and the layer thicknesses of aperiodic multilayer structures. In Section III, we discuss the properties of the structures with ultrabroadband near-perfect absorption in the visible and near-infrared, which we obtain with the optimization algorithm. Finally, our conclusions are summarized in Section IV.

2. Theory

We consider aperiodic multilayer structures composed of infinite slabs of material of varying thicknesses above a semi-infinite silicon substrate. For each layer, the material is chosen among magnesium fluoride (MgF_2), titanium dioxide (TiO_2), hafnium dioxide (HfO_2), chromium (Cr), tungsten (W), germanium (Ge), and silicon (Si). Light is incident from the air at an angle θ to the structure. We use experimental data for the wavelength-dependent complex indices of refraction for all materials considered in this paper [4], [39], [40]. Using the transfer matrix method [41], we calculate the transmission and reflection of each multilayer structure for both TE and TM polarized light. Once the transmission and reflection are calculated, the absorption can be obtained using

$$A_{\text{TE/TM}}(\lambda, \theta) = 1 - R_{\text{TE/TM}}(\lambda, \theta) - T_{\text{TE/TM}}(\lambda, \theta), \tag{1}$$

where $A_{\text{TE/TM}}$ is the TE/TM absorption, $R_{\text{TE/TM}}$ is the TE/TM reflection, $T_{\text{TE/TM}}$ is the TE/TM transmission, and λ is the wavelength. The transmission, reflection, and absorption of each multilayer structure can also be calculated using the impedance method [42].

We use a hybrid optimization algorithm, coupled with the transfer-matrix method, to optimize both the material composition and the layer thicknesses. In order to achieve ultrabroadband near-perfect absorption, we considered a broad range of materials, including dielectrics such as MgF_2, HfO_2, and TiO_2, metals such as Cr and W, and semiconductors such as Si and Ge. By considering such a broad range of materials, our optimization algorithm can identify appropriate structures, which exhibit near-perfect absorption over the selected wavelength range. Each of the absorbing materials used leads to near-perfect absorption at specific wavelength ranges. We also note that other absorbing metals and dielectric materials with similar refractive index spectra can be used [4].

Our goal is to maximize the wavelength range $\lambda_2 - \lambda_1$ over which the absorption for normally incident light $A(\lambda, \theta = 0°)$ is continuously larger than 90%. Here, λ_1 and λ_2 are the lower and upper absorption band edges, respectively, and we choose $\lambda_1 = 400$ nm.

While several approaches have been proposed to optimize the geometrical dimensions of multilayer photonic nanostructures, with a given material composition, very few works have considered simultaneously optimizing the material composition and dimensions of such nanostructures [5], [12]. Here, we use a hybrid optimization algorithm as a method to design optimal multilayer photonic structures. Leveraging recent progress in metaheuristic optimization, we develop an optimization method consisting of three stages: a Monte Carlo simulation, a continuous adaptive genetic algorithm, and a pattern search algorithm. The first stage identifies the best material compositions. The second and third stages optimize the thicknesses for each material composition.

In the first stage of the optimization procedure, we perform a Monte Carlo simulation over the entire design space. We randomly generate a large number of structures within the constraints of the design problem. Typically, we generate 15 million random structures. This number of structures is necessary in order to identify the best material compositions. These multilayer structures have a random material and a random thickness chosen for each layer. Structures are ranked according to the fitness function, which, as mentioned above, is the bandwidth over which the absorption for normally incident light is continuously larger than 90%. We find that the Monte Carlo simulation yields viable material compositions. The material compositions of the best n structures are used to parameterize the genetic algorithm in the next stage. Typically, we choose $n = 20$.

In the second stage of the optimization procedure, n genetic algorithm populations are generated; one for each material composition obtained in the previous stage. The population size is chosen to be 60. To optimize their thicknesses, these populations, each with a different fixed material composition, are run in parallel for a number of generations, evaluating the structures of each generation and using the characteristics of those that best satisfy the fitness function to improve other structures. For each population, the genetic algorithm iteratively generates a new generation by the application of selection, crossover, and mutation operators. Each population converges towards the optimum of its solution space. We typically run 2000 generations for each population. The genetic algorithm that we use is continuous [43], because the parameters (in this case the layer thicknesses) are treated as continuous variables, rather than bitstring chromosomes as in classical genetic algorithms. The genetic algorithm that we use is also adaptive [44], because it uses characteristics of the population pool to guide optimization. More specifically, the adaptive genetic algorithm that we use dynamically varies the crossover probability and mutation probability during the simulation, based on the observed convergence of the population, instead of using fixed values for each.

In the third stage of the optimization procedure, we apply a pattern search local optimization algorithm to the best result from each population obtained from the genetic algorithm, to find the exact optimum. More specifically, the structures obtained from the genetic algorithm are locally optimized with the Hooke-Jeeves pattern search algorithm [45]. The pattern search algorithm that we use in the third stage, which is a local optimization algorithm, is more effective at finding the exact optimum, compared to the genetic algorithm used in the second stage, which is a global optimization algorithm.

We note here that in all cases we found that the optimal structures are unique. In other words, if the stochastic optimization procedure is repeated, it converges to the same result. We also note that optimization algorithms previously used to design ultrabroadband near-perfect absorbers only optimized the layer thicknesses of structures with fixed material composition. In contrast, as we will show below, our approach of simultaneously optimizing the material composition as well as the layer thicknesses leads to structures with broader near-perfect absorption.

3. Results

Here we consider structures with five, seven, nine, and eleven layers. In each of these cases, we use the optimization algorithm, described in the previous section, to maximize the wavelength range
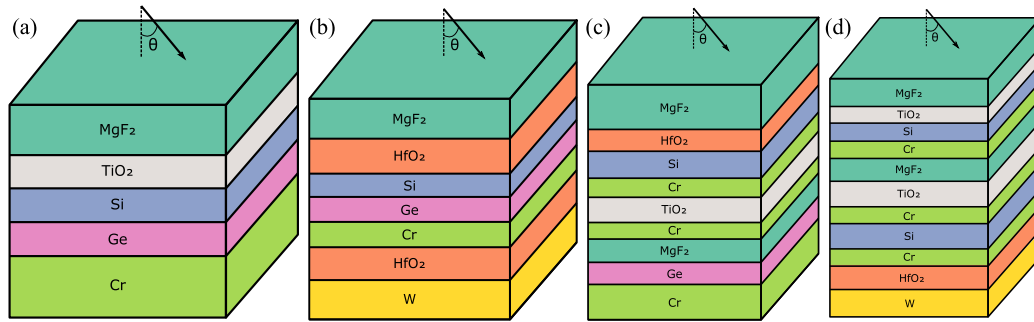
Fig. 1. Schematics of the multilayer structures with optimized material composition. The schematics in (a), (b), (c), and (d) show the optimized material composition for five-, seven-, nine-, and eleven-layer structures, respectively. For each layer, the material is chosen among magnesium fluoride (MgF$_2$), titanium dioxide (TiO$_2$), hafnium dioxide (HfO$_2$), chromium (Cr), tungsten (W), germanium (Ge), and silicon (Si).
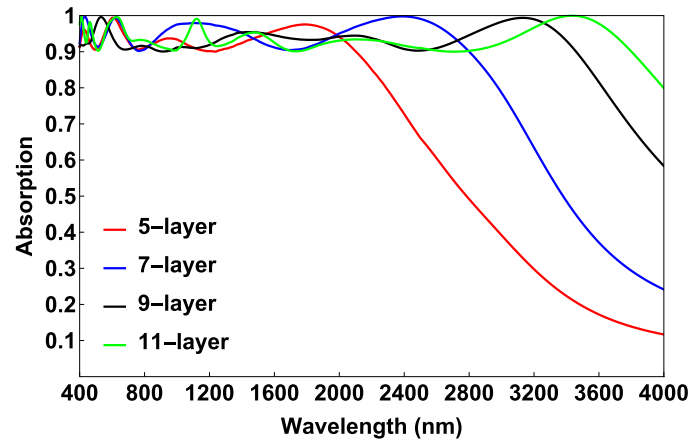

Fig. 2. Absorption for normally incident light, $A(\lambda, \theta = 0°)$, as a function of wavelength for the optimized five-, seven-, nine-, and eleven-layer structures. The optimized material composition for the five-, seven-, nine-, and eleven-layer structures is shown in Figs. 1(a), 1(b), 1(c), and 1(d), respectively. The optimized layer thicknesses, in units of nanometers, beginning with the layer bordering air are: {143, 52, 29, 39, 220} for the five-layer structure, {141, 56, 33, 47, 30, 134, 190} for the seven-layer structure, {244, 59, 47, 7, 88, 8, 132, 124, 392} for the nine-layer structure, and {123, 53, 22, 6, 140, 199, 7, 128, 23, 239, 724} for the eleven-layer structure.

$\lambda_2 - \lambda_1$ over which the absorption for normally incident light $A(\lambda, \theta = 0°)$ is continuously larger than 90%. In other words, the merit function during the optimization procedure is $\lambda_2 - \lambda_1$. Here, we choose $\lambda_1 = 400$ nm. As mentioned above, our algorithm simultaneously optimizes the material composition as well as the layer thicknesses of each structure.

Fig. 1 shows the optimized material composition for five-, seven-, nine-, and eleven-layer structures. As mentioned above, for each layer, the material is chosen among magnesium fluoride, titanium dioxide, hafnium dioxide, chromium, tungsten, germanium, and silicon. We note that, in all cases, we found that, in the structures with optimized material composition, the material in the bottom layer (the one adjacent to the silicon substrate) is a metal; either chromium or tungsten. In addition, we found that in all cases this bottom metallic layer is thick enough, so that light does not penetrate into the silicon substrate below the metallic layer. Thus, this thick metallic bottom layer acts as a semi-infinite metallic substrate. In the schematics of Fig. 1, we therefore do not show the silicon substrate, since it does not affect the absorption properties of the structures.
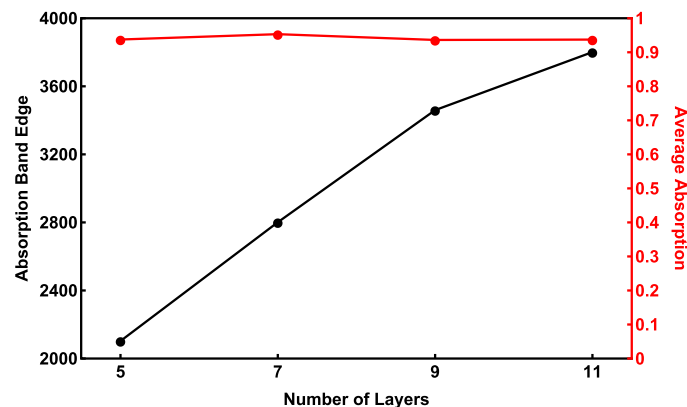
Fig. 3. Upper absorption band edge λ_2 as a function of the number of layers of the optimized structures described in Fig. 2. Also shown is the average absorption in the wavelength range between the lower (λ_1) and upper (λ_2) absorption band edges as a function of the number of layers of the optimized structures described in Fig. 2.

Fig. 2 shows the absorption for normally incident light $A(\lambda, \theta = 0°)$ as a function of wavelength for the optimized five-, seven-, nine-, and eleven-layer structures. The optimized material composition of each structure is shown in Fig. 1, while the optimized layer thicknesses are given in the caption of Fig. 2. We note here that, as expected, as the number of layers increases, the time required for our optimization procedure to converge increases. We observe that the bandwidth over which high absorption (>90%) is achieved increases with the number of layers. This is further illustrated in Fig. 3, which shows the upper absorption band edge λ_2 as a function of the number of layers for the optimized structures, described in Fig. 2. The upper absorption band edge λ_2 is 2103 nm, 2801 nm, 3460 nm, and 3801 nm for the five-, seven-, nine-, and eleven-layer structures, respectively. Note that, as mentioned above, in all cases the lower absorption band edge is $\lambda_1 = 400$ nm. Fig. 3 also shows the average absorption in the wavelength range between the lower (λ_1) and upper (λ_2) absorption band edges as a function of the number of layers. In all cases, the average absorption is slightly above the 90% threshold. More specifically, the average absorption is 93.75%, 95.32%, 93.62%, and 93.73% for the five-, seven-, nine-, and eleven-layer structures, respectively.

It is worth noting that the optimized material composition for the five-layer structure is the same as the one in Ref. [4]. However, the optimized layer thicknesses are slightly different, since in our case we maximize the wavelength range over which the absorption is continuously larger than 90%, instead of maximizing the average absorption over a fixed wavelength range. We also note that simultaneously optimizing the material composition, as well as the layer thicknesses, leads to structures with broader near-perfect absorption. More specifically, the bandwidth over which high absorption (>90%) is achieved is ~3100 nm and ~3400 nm for nine-, and eleven-layer structures, respectively (Fig. 3). In comparison, when optimizing the layer thicknesses of structures with fixed material composition, the bandwidth over which high absorption (>90%) is achieved is ~2700 nm and ~3100 nm for nine-, and eleven-layer structures, respectively [4].

As mentioned above, the multilayer structures were optimized to maximize the wavelength range over which the absorption is continuously larger than 90% for normally incident light. Now, we consider the angular dependence of the absorption. More specifically, in Fig. 4 we show absorption as a function of wavelength and angle for the optimized seven-layer structure of Fig. 1(b). The absorption under unpolarized light is the average absorption over the TE and TM polarizations [5]. We observe that, even though the structures were optimized for normally incident light, the absorption is high in a broad angular range within the wavelength range of interest. More specifically, the average absorption in the wavelength range between the lower (λ_1) and upper (λ_2) absorption band edges is more than 90% when the angle of incidence is up to 60°, and more than 80% when the angle of incidence is up to 70°.
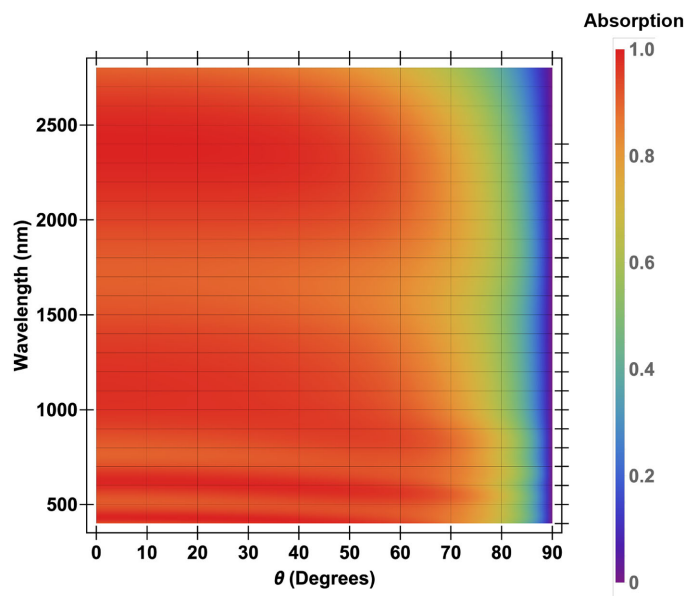
Fig. 4. Absorption as a function of wavelength and angle for the optimized seven-layer structure of Fig. 1(b). The optimized layer thicknesses are given in Fig. 2.
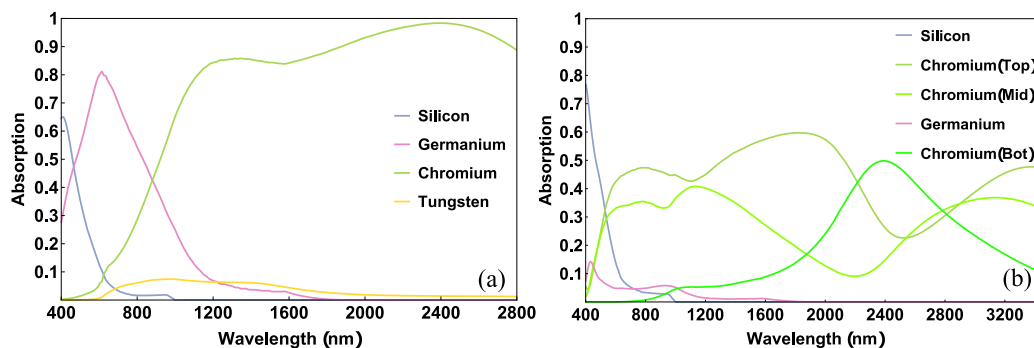

Fig. 5. (a) Ratio of the power absorbed inside each absorbing layer to the total normally incident power on the optimized seven-layer structure of Fig. 1(b) as a function of wavelength. The optimized layer thicknesses are given in Fig. 2. (b) Ratio of the power absorbed inside each absorbing layer to the total normally incident power on the optimized nine-layer structure of Fig. 1(c) as a function of wavelength. The optimized layer thicknesses are given in Fig. 2.

We now explain the physical origin of ultrabroadband absorption. More specifically, to better understand how the optimized multilayer structures achieve high absorption in a broad wavelength range, we investigate how much power is absorbed inside each absorbing layer. For the optimized seven-layer [Fig. 1(b)] and nine-layer [Fig. 1(c)] structures, the absorbing layers are the Si, Ge, Cr, and W layers. In Figs. 5(a) and 5(b), we show the calculated ratio of the power absorbed inside each of these absorbing layers, to the total normally incident power on the optimized seven-layer and nine-layer structures of Figs. 1(b) and 1(c), respectively, as a function of wavelength. We observe that, even though these two structures use the same absorbing materials, the absorption characteristics of the structures are quite different. In the seven-layer structure absorption in the germanium layer dominates in a quite broad wavelength range [Fig. 5(a)]. On the other hand, in the nine-layer structure the absorption in the germanium layer is low in the entire wavelength
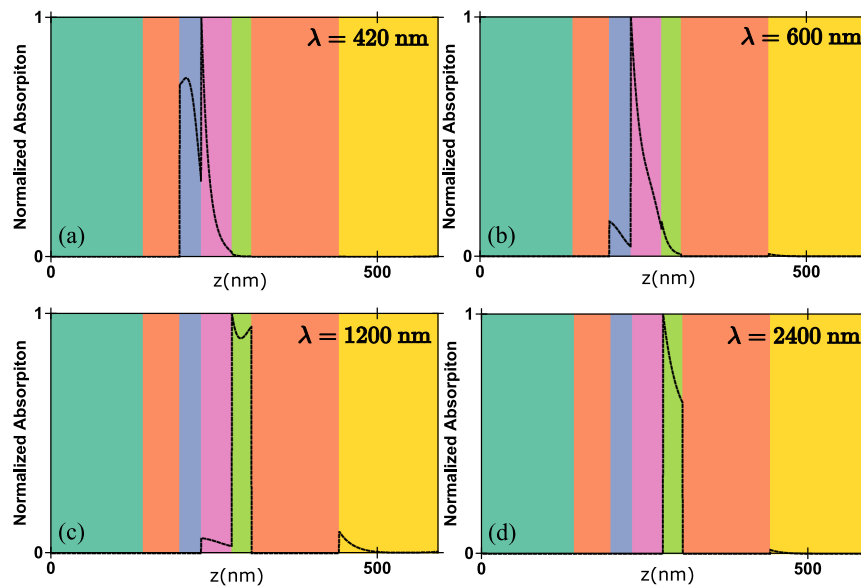
Fig. 6. (a) Profile of the absorption distribution for the optimized seven-layer structure of Fig. 1(b) at $\lambda = 420$ nm. The structure is excited by a normally incident plane wave. We also calculated the ratio of the power absorbed inside each layer to the total normally incident power on the structure and from left to right is: {0, 0, 0.638, 0.346, 0.003, 0, 0}. (b) Same as in (a) except that $\lambda = 600$ nm. The ratio of the power absorbed inside each layer to the total normally incident power on the structure from left to right is: {0, 0, 0.126, 0.798, 0.056, 0, 0.007}. (c) Same as in (a) except that $\lambda = 1200$ nm. The ratio of the power absorbed inside each layer to the total normally incident power on the structure from left to right is: {0, 0, 0, 0.069, 0.843, 0, 0.064}. (d) Same as in (a) except that $\lambda = 2400$ nm. The ratio of the power absorbed inside each layer to the total normally incident power on the structure from left to right is: {0, 0, 0, 0, 0.983, 0, 0.014}.

range of interest [Fig. 5(b)]. In the seven-layer structure the silicon and germanium layers absorb most of the power at shorter wavelengths [Fig. 5(a)]. As the wavelength increases, germanium and silicon gradually become less absorbing and absorption in the chromium layer dominates. In the nine-layer structure the silicon layer is the most absorbing layer for wavelengths up to ∼530 nm [Fig. 5(b)]. At longer wavelengths the incident power is mostly absorbed in the three chromium layers. We observe that having multiple absorbing layers extends the bandwidth over which high absorption (>90%) is achieved. In the seven-layer structure there is only one chromium layer and the absorption is above 90% for wavelengths up to 2801 nm (Fig. 3). In comparison, in the nine-layer structure there are three chromium layers, which all significantly contribute to the overall power absorbed by the structure. Through these three chromium layers, the bandwidth over which high absorption is achieved is extended, so that the absorption is above 90% for wavelengths up to 3460 nm (Fig. 3).

To further understand the absorption properties of the structures and the physical origin of ultrabroadband absorption, in Fig. 6 we plot the profile of the absorption distribution for the seven-layer structure of Fig. 1(b) at different wavelengths, when the structure is excited by a normally incident plane wave. In addition, the ratio of the power absorbed inside each layer, to total normally incident power on the structure at different wavelengths, is given in the caption of Fig. 6. At the wavelength of 420 nm the silicon and germanium layers absorb ∼98.4% of the incident power [Fig. 6(a)]. This is due to the fact that the extinction coefficients of silicon and germanium are relatively large in the wavelength range between 400 nm and 500 nm [4]. As the wavelength increases, the silicon layer becomes less absorbing because the extinction coefficient of silicon decreases [4]. Thus, at the wavelength of 600 nm, the germanium layer absorbs ∼79.8% of the

incident power [Fig. 6(b)]. As the wavelength further increases, silicon becomes transparent and the extinction coefficient of germanium decreases, while the extinction coefficient of chromium increases [4]. Thus, at the wavelength of 1200 nm the chromium layer absorbs $\sim$84.3% of the incident power, while the germanium and tungsten layers absorb $\sim$6.9% and $\sim$6.4%, respectively, of the incident power [Fig. 6(c)]. At even longer wavelengths, germanium becomes transparent, so that at 2400 nm the chromium layer absorbs $\sim$98.3% of the incident power [Fig. 6(d)].

4. Summary

In this paper, we presented aperiodic multilayer structures with ultrabroadband near-perfect absorption in the visible and near-infrared wavelength range. This range is important for many applications related to solar photovoltaics, imaging, and photodetection. We used a hybrid optimization algorithm coupled with the transfer-matrix method, to optimize both the material composition and the layer thicknesses of the aperiodic multilayer structures that are composed of infinite slabs of material above a semi-infinite substrate. We note that optimization algorithms previously used to design ultrabroadband near-perfect absorbers only optimized the layer thicknesses of structures with fixed material composition. In contrast, we found that our approach of simultaneously optimizing the material composition as well as the layer thicknesses leads to structures with broader near-perfect absorption. Our algorithm maximized the wavelength range $\lambda_2 - \lambda_1$ over which the absorption for normally incident light is continuously larger than 90% with a lower absorption band edge of $\lambda_1 =$400 nm. In order to achieve ultrabroadband near-perfect absorption, we considered a broad range of materials including dielectrics such as magnesium fluoride, hafnium dioxide, and silicon dioxide, metals such as chromium, tungsten, and silver, and semiconductors such as silicon and germanium.

Our hybrid optimization algorithm consists of three stages: a Monte Carlo simulation, a continuous adaptive genetic algorithm, and a pattern search algorithm. We first perform a Monte Carlo simulation over the entire design space. We generate a large number of structures with a random material and a random thickness chosen for each layer. The material compositions of the best structures are used to parameterize the genetic algorithm in the next stage. One genetic algorithm population is generated for each material composition obtained in the previous stage. These populations, each with a different fixed material composition, are run in parallel and converge towards the optimum of their solution space typically after a few thousand generations. We finally apply a pattern search local optimization algorithm to the best result from each population obtained from the genetic algorithm to find the exact optimum.

In this paper, we considered structures with five, seven, nine, and eleven layers. We found that the bandwidth over which near-perfect absorption is achieved increases with the number of layers. In addition, simultaneously optimizing the material composition as well as the layer thicknesses leads to structures with broader near-perfect absorption. The upper absorption band edge λ_2 is 2103 nm, 2801 nm, 3460 nm, and 3801 nm for the five-, seven-, nine-, and eleven-layer structures, respectively. We also found that, even though the structures were optimized for normally incident light, the absorption is high in a broad angular range within the wavelength range of interest.

We also explained the physical origin of ultrabroadband absorption. More specifically, to better understand how the optimized multilayer structures achieve high absorption in a broad wavelength range, we investigated how much power is absorbed inside each absorbing layer. We found that, even though all structures use the same absorbing materials, the absorption characteristics of the optimized structures with different number of layers are quite different.

As final remarks, we note that the optimized multilayer structures can be fabricated by simple film deposition methods such as e-beam evaporation [4]. For structures fabricated with such methods the calculated absorption spectra using the transfer matrix method are in excellent agreement with the measured absorption spectra [4]. Thus, we expect that, if the optimized multilayer structures presented in this paper are fabricated with such methods, their absorption spectra will be in excellent agreement with the calculated spectra shown in Fig. 2.

References

[1] N. Liu, M. Mesch, T. Weiss, M. Hentschel, and H. Giessen, "Infrared perfect absorber and its application as plasmonic sensor," *Nano Lett.*, vol. 10, no. 7, pp. 2342–2348, 2010.

[2] H. Kwon and S. Kim, "Chemically tunable, biocompatible, and cost-effective metal-insulator-metal resonators using silk protein and ultrathin silver films," *ACS Photon.*, vol. 2, no. 12, pp. 1675–1680, 2015.

[3] A. Tittl, P. Mai, R. Taubert, D. Dregely, N. Liu, and H. Giessen, "Palladium-based plasmonic perfect absorber in the visible wavelength range and its application to hydrogen sensing," *Nano Lett.*, vol. 11, no. 10, pp. 4366–4369, 2011.

[4] C. Yang *et al.*, "Compact multilayer film structures for ultrabroadband, omnidirectional, and efficient absorption," *ACS Photon.*, vol. 3, no. 4, pp. 590–596, 2016.

[5] Y. Shi, W. Li, A. Raman, and S. Fan, "Optimization of multilayer optical films with a memetic algorithm and mixed integer programming," *ACS Photon.*, vol. 5, no. 3, pp. 684–691, 2018.

[6] X. Liu, T. Tyler, T. Starr, A. F. Starr, N. M. Jokerst, and W. J. Padilla, "Taming the blackbody with infrared metamaterials as selective thermal emitters," *Phys. Rev. Lett.*, vol. 107, 2011, Art. no. 045901.

[7] S. S. Mirshafieyan and D. A. Gregory, "Electrically tunable perfect light absorbers as color filters and modulators," *Sci. Rep.*, vol. 8, no. 1, 2018, Art. no. 2635.

[8] M. A. Kats, R. Blanchard, P. Genevet, and F. Capasso, "Nanometre optical coatings based on strong interference effects in highly absorbing media," *Nat. Mater.*, vol. 12, pp. 20–24, 2012.

[9] S. G. Lorenzo, C. You, C. H. Granier, G. Veronis, and J. P. Dowling, "Optimized mid-infrared thermal emitters for applications in aircraft countermeasures," *AIP Adv.*, vol. 7, no. 12, a2017, Art. no. 125112.

[10] C. H. Granier, S. G. Lorenzo, C. You, G. Veronis, and J. P. Dowling, "Optimized aperiodic broadband visible absorbers," *J. Opt.*, vol. 19, no. 10, 2017, Art. no. 105003.

[11] C. H. Granier, F. O. Afzal, C. Min, J. P. Dowling, and G. Veronis, "Optimized aperiodic highly directional narrowband infrared emitters," *J. Opt. Soc. Am. B*, vol. 31, no. 6, pp. 1316–1321, 2014.

[12] C. H. Granier, F. O. Afzal, S. G. Lorenzo, M. Reyes Jr, J. P. Dowling, and G. Veronis, "Optimized aperiodic multilayer structures for use as narrow-angular absorbers," *J. Appl. Phys.*, vol. 116, no. 24, 2014, Art. no. 243101.

[13] J. Chen, J. Guo, and L.-Y. Chen, "Super-wideband perfect solar light absorbers using titanium and silicon dioxide thin-film cascade optical nanocavities," *Opt. Mater. Express*, vol. 6, no. 12, pp. 3804–3813, 2016.

[14] Y. Huang *et al.*, "Catenary electromagnetics for ultra-broadband lightweight absorbers and large-scale flat antennas," *Adv. Sci.*, vol. 6, 2019, Art. no. 1801691.

[15] H. Deng *et al.*, "Broadband perfect absorber based on one ultrathin layer of refractory metal," *Opt. Lett.*, vol. 40, no. 11, pp. 2592–2595, 2015.

[16] J. Park, S. J. Kim, and M. L. Brongersma, "Condition for unity absorption in an ultrathin and highly lossy film in a gires-tournois interferometer configuration," *Opt. Lett.*, vol. 40, no. 9, pp. 1960–1963, 2015.

[17] Y. Huang, L. Liu, M. Pu, X. Li, X. Ma, and X. Luo, "A refractory metamaterial absorber for ultra-broadband, omnidirectional and polarization-independent absorption in the UV-NIR spectrum," *Nanoscale*, vol. 10, pp. 8298–8303, 2018.

[18] H. Zhang, L. Feng, Y. Liang, and T. Xu, "An ultra-flexible plasmonic metamaterial film for efficient omnidirectional and broadband optical absorption," *Nanoscale*, vol. 11, pp. 437–443, 2019.

[19] Y. Gong *et al.*, "Highly efficient and broadband mid-infrared metamaterial thermal emitter for optical gas sensing," *Opt. Lett.*, vol. 42, no. 21, pp. 4537–4540, 2017.

[20] C. You, A. Nellikka, I. De Leon, and O. S. Magaña-Loaiza, "Multiparticle quantum plasmonics," *Nanophotonics*, to be published.

[21] J. Ma, J. Wang, Z. Hu, Z. Zhang, L. Pan, and A. Di Falco, "High-efficiency and ultrabroadband flexible absorbers based on transversely symmetrical multi-layer structures," *AIP Advances*, vol. 9, 2019, Art. no. 115007.

[22] M. R. S. Dias, C. Gong, Z. A. Benson, and M. S. Leite, "Lithography–free, omnidirectional, CMOS–compatible AlCu alloys for thin–film superabsorbers," *Adv. Opt. Mater.*, vol. 6, 2018, Art. no. 1700830.

[23] Y. Huang, C. Min, and G. Veronis, "Broadband near total light absorption in non-PT-symmetric waveguide-cavity systems," *Opt. Express*, vol. 24, no. 19, pp. 22 219–22 231, 2016.

[24] B. J. Lee and Z. M. Zhang, "Design and fabrication of planar multilayer structures with coherent thermal emission characteristics," *J. Appl. Phys.*, vol. 100, no. 6, 2006, Art. no. 063529.

[25] S. Martin, J. Rivory, and M. Schoenauer, "Synthesis of optical multilayer systems using genetic algorithms," *Appl. Opt.*, vol. 34, no. 13, pp. 2247–2254, 1995.

[26] E. Michielssen, J. Sajer, S. Ranjithan, and R. Mittra, "Design of lightweight, broad-band microwave absorbers using genetic algorithms," *IEEE Trans. Microw. Theory Techn.*, vol. 41, no. 6, pp. 1024–1031, Jun.–Jul. 1993.

[27] D. J. Poxson, M. F. Schubert, F. W. Mont, E. F. Schubert, and J. K. Kim, "Broadband omnidirectional antireflection coatings optimized by genetic algorithm," *Opt. Lett.*, vol. 34, no. 6, pp. 728–730, 2009.

[28] R. I. Rabady and A. Ababneh, "Global optimal design of optical multilayer thin-film filters using particle swarm optimization," *Optik*, vol. 125, no. 1, pp. 548–553, 2014.

[29] M. P. Hobson and J. E. Baldwin, "Markov-chain monte carlo approach to the design of multilayer thin-film optical coatings," *Appl. Opt.*, vol. 43, no. 13, pp. 2651–2660, 2004.

[30] O. Ilic, P. Bermel, G. Chen, J. D. Joannopoulos, I. Celanovic, and M. Soljačić, "Tailoring high-temperature radiation and the resurrection of the incandescent source," *Nat. Nanotechnol.*, vol. 11, pp. 320–324, 2016.

[31] A. V. Tikhonravov, M. K. Trubetskov, and G. W. DeBell, "Optical coating design approaches based on the needle optimization technique," *Appl. Opt.*, vol. 46, no. 5, pp. 704–710, 2007.

[32] L. Li, Q.-H. Wang, D.-H. Li, and H.-R. Peng, "Jump method for optical thin film design," *Opt. Express*, vol. 17, no. 19, pp. 16 920–16 926, 2009.

[33] A. Jiang, O. Yoshie, and L. Chen, "A new multilayer optical film optimal method based on deep q-learning," 2018, *arXiv:1812.02873*.

[34] J. Peurifoy *et al.*, "Nanophotonic particle simulation and inverse design using artificial neural networks," *Sci. Adv.*, vol. 4, no. 6, 2018, Paper eaar4206.

[35] D. Liu, H. Yu, Z. Yang, and Y. Duan, "Ultrathin planar broadband absorber through effective medium design," *Nano Res.*, vol. 9, no. 8, pp. 2354–2363, 2016.

[36] C. S. Solanki, *Solar Photovoltaics: Fundamentals, Technologies and Applications*. Delhi, India: PHI Learning Pvt. Ltd., 2015.

[37] T. Rauch *et al.*, "Near-infrared imaging with quantum-dot-sensitized organic photodiodes," *Nat. Photon.*, vol. 3, no. 6, pp. 332–336, 2009.

[38] H. Liu, "Quantum dot infrared photodetector," *Opto-Electron. Rev.*, vol. 11, no. 1, pp. 1–5, 2003.

[39] D. R. Lide, *CRC Handbook of Chemistry and Physics*. Boca Raton, FL, USA: CRC Press, 2004, vol. 85.

[40] E. D. Palik, *Handbook of Optical Constants of Solids*. New York, NY, USA: Academic, 1997.

[41] P. Yeh, *Optical Waves in Layered Media*. Hoboken, NJ, USA; Wiley, 1988, vol. 95.

[42] H. A. Haus, *Waves and Fields in Optoelectronics*. Englewood Cliffs, NJ, USA: Prentice–Hall, 1983.

[43] R. Chelouah and P. Siarry, "A continuous genetic algorithm designed for the global optimization of multimodal functions," *J. Heuristics*, vol. 6, no. 2, pp. 191–213, 2000.

[44] N. L. Law and K. Y. Szeto, "Adaptive genetic algorithm with mutation and crossover matrices," in *Proc. Int. Joint Conf. Artif. Intell.*, 2007, pp. 2330–2333.

[45] R. Hooke and T. A. Jeeves, "Direct search solution of numerical and statistical problems," *J. ACM*, vol. 8, no. 2, pp. 212–229, 1961.